Why did deep convection persist over four consecutive winters (2015-2018) Southeast of Cape Farewell?

Patricia ZUNINO[1], Herlé MERCIER[2] and Virginie THIERRY[3].

1 Altran Technologies, Technopôle Brest Iroise, Site du Vernis , 300 rue Pierre Rivoalon, 29200 Brest, France

2 CNRS, University of Brest, IRD, Ifremer, Laboratoire d'Océanographie Physique et Spatiale (LOPS), IUEM, ZI de la pointe du diable, CS 10070 - 29280 Plouzané, France

3 Ifremer, University of Brest, CNRS, IRD, Laboratoire d'Océanographie Physique et Spatiale (LOPS), IUEM, ZI de la pointe du diable, CS 10070 - 29280 Plouzané, France

Corresponding author: patricia.zuninorodriguez@altran.fr

ABSTRACT

After more than a decade of shallow convection, deep convection returned to the Irminger Sea in 2008 and occurred several times since then to reach exceptional convection depths (>1,500 m) in 2015 and 2016. Additionally, deep mixed layers larger than 1600 m were also reported Southeast of Cape Farewell in 2015. In this context, we used Argo data to show that deep convection occurred Southeast of Cape Farewell (SECF) in 2016 and persisted during two additional years in 2017 and 2018 with maximum convection depth larger than 1,300 m. In this article, we investigate the respective roles of air-sea buoyancy flux and preconditioning of the water column (ocean interior buoyancy content) to explain this exceptional 4-year persistence of deep convection SECF. We analyzed the respective contributions of the heat and freshwater components. Contrary to the very negative air-sea buoyancy flux that was observed during winter 2015, the buoyancy fluxes over the SECF region during winters 2016, 2017 and 2018 were close to the climatological average. We estimated the preconditioning of the water column as the buoyancy that needs to be removed (B) from the end of summer water column to homogenize it down to a given depth. B was lower for winters 2016 – 2018 than for the 2008 – 2015 winter mean, due especially to a vanishing stratification from 600 m down to ~1,300 m. It means that less air-sea buoyancy loss was necessary to reach a given convection depth than in the mean and once convection reached 600 m little additional buoyancy loss was needed to homogenize the water column down to 1,300 m. We showed that the decrease in B was due to the combined effects of the local cooling of the intermediate water (200 – 800 m) and the advection of a negative S anomaly in the 1,200 – 1,400 m layer. This favorable preconditioning permitted the very deep convection observed in 2016 – 2018 despite the atmospheric forcing was close to the climatological average.

1. INTRODUCTION

Deep convection is the result of a process by which surface waters loose buoyancy due to atmospheric forcing and sink into the interior of the ocean. It occurs only where specific conditions are met including large air-sea buoyancy loss and favorable preconditioning (i.e. low stratification of the water column) (Marshall & Schott, 1999). In the Subpolar North Atlantic (SPNA), deep convection takes place in the Labrador Sea, South of Cape Farewell and in the Irminger Sea (Kieke & Yashayaev, 2015; Pickart et al. 2003; Piron et al. 2017). Deep convection connects the upper and lower limbs of the Meridional Overturning Circulation (MOC) and transfers climate change signals from the surface to the ocean interior.

Observing deep convection is difficult because it happens on short time and small spatial scales and during periods of severe weather conditions (Marshall & Schott, 1999). The onset of the Argo program at the beginning of the 2000s has considerably increased the number of available oceanographic data throughout the year. Although the sampling characteristics of Argo are not adequate to observe the small scales associated with the convection process itself, Argo data allow the description of the overall intensity of the event and the characterization of the properties of the water masses formed in the winter mixed layer as well (e.g., Yashayaev and Loder, 2017).

In the Labrador Sea, deep convection occurs every year, yet with different intensity (e.g., Yashayaev and Clarke, 2008; Kieke and Yashayaev, 2015). In the Irminger Sea, Argo and mooring data showed that convection deeper than 700 m happened during winters 2008, 2009, 2012, 2015 and 2016 (Väge et al., 2009; de Jong et al., 2012; Piron et al. 2015; de Jong & de Steur, 2016; Fröb et al., 2016; Piron et al. 2017; de Jong et al., 2018). Moreover, in winter 2015, deep convection was also observed south of Cape Farewell (Piron et al., 2017). Excluding winter 2009 when the deep convection event was made possible thanks to a favorable preconditioning (de Jong et al., 2012), all events coincided with strong atmospheric forcing (air-sea heat loss). Prior to 2008, only few deep convection events were reported because the mechanisms leading to it were not favorable (Centurioni and Gould, 2004) or because the observing system was not adequate (Bacon, 1997; Pickart et al., 2003). Nevertheless, the hydrographic properties from the 1990s suggested that deep convection reached as deep as 1,500 m in the Irminger Sea during winters 1994 and 1995 (Pickart et al., 2003), and as deep as 1,000 m south of Cape Farewell during winter 1997 (Bacon et al., 2003).

The convection depths that were reached in the Irminger Sea and south of Cape Farewell at the end of winter 2015 were the deepest observed in these regions since the beginning of the 21st century (de Jong et al., 2016; Piron et al., 2017, Fröb et al., 2016). In this work, we show that deep convection

103   also happened in a region between south of Cape Farewell and the Irminger Sea (the pink box in

104   Figure 1) every winter from 2016 to 2018. Hereinafter, we will refer to this region as Southeast Cape

105   Farewell (SECF). We investigated the respective role of atmospheric forcing (air-sea buoyancy flux)

106   and preconditioning (ocean interior buoyancy content) in setting the convection intensity. We also

107   disentangled the relative contribution of salinity and temperature anomalies to the preconditioning.

108   The paper is organized as follow. The data are described in Sect. 2. The methodology is explained in

109   Sect. 3. We expose our results in Sect. 4 and discuss them in Sect. 5. Conclusions are listed in Sect. 6.

110

111   2. DATA

112   We used temperature (T), salinity (S) and pressure (P) data measured by Argo floats north of 55°N in

113   the Atlantic Ocean. These data were collected by the International Argo program

114   (http://www.argo.ucsd.edu/), http://www.jcommops.org/) and downloaded from the Coriolis Data

115   Center (http://www.coriolis.eu.org/). Only data flagged as good (quality Control < 3, Argo Data

116   Management Team, 2017) were considered in our analysis. Potential temperature (θ), density (ρ)

117   and potential density anomaly referenced to the surface and 1000 dbar (σ_0 and σ_1, respectively) were

118   estimated from T, S and P data using TEOS-10 (http://www.teos-10.org/).

119   We used two different gridded products of ocean T and S: ISAS and EN4. ISAS (Gaillard et al., 2016;

120   Kolodziejczyk et al., 2017) is produced by optimal interpolation of *in situ* data. It provides monthly

121   fields, at 152 depth levels, at 0.5° resolution, from 2002 to 2015. Near real time data are also

122   availaible for 2016 and 2018. EN4 (Good et al., 2013) is an optimal interpolation of *in situ* data; it

123   provides monthly T and S at 1° spatial resolution and at 42 depth levels, for the period 1900 to

124   present.

125   Net air-sea heat flux (Q , the sum of radiative and turbulent fluxes), evaporation (E), precipitation (P),

126   wind stress (τ_x and τ_y) and sea surface temperature (SST) data were obtained from ERA-Interim

127   reanalysis (Dee et al., 2011). ERA-Interim provides data with a time resolution of 12h and a spatial

128   resolution of 0.75°, respectively. The air-sea freshwater flux (FWF) was estimated as E - P.

129   We used monthly Absolute Dynamic Topographic (ADT), which was computed from the daily 0.25° -

130   resolution ADT data provided by CMEMS (Copernicus Marine and Environment Monitoring Service,

131   http://www.marine.copernicus.eu).

132

133   3. METHODS

3.1 Quantification of the deep convection

We characterized the convection in the SPNA in winters 2015-2018 by estimating the mixed layer depths (MLD) for all Argo profiles collected in the SPNA north of 55°N from 1st January to 30th April of each year (Fig. 1). The MLD was estimated as the shallowest of the three MLD estimates obtained by applying the threshold method (de Boyer Montégut et al., 2004) to θ, S and ρ profiles separately. The threshold method computes the MLD as the depth at which the difference between the surface (30 m) and deeper levels in a given property is equal to a given threshold. In case visual inspection of the winter profiles showed a thin stratified layer at the surface, a slightly deeper level (<150 m) was considered as surface reference level. Following Piron et al. (2017), this threshold was taken equal to 0.01 kg m^{-3} for ρ. For θ and S, we selected thresholds of 0.1°C and 0.012 respectively because they correspond to the threshold of 0.01 kg m^{-3} in ρ. The latter was previously shown to perform well in the subpolar gyre on density profiles (Piron et al., 2016). Our MLD estimates are comparable to those obtained using MLD determination based on Pickart et al. (2002)'s and de Jong et al. (2012)'s methods (see section S1, Fig. S1 and Fig. S2 in supplementary material).

In this paper, deep convection is characterized by profiles with MLD deeper than 700m (colored points in Fig. 1) because it is the minimum depth that should be reached for renewing Labrador Sea Water (LSW) (Yashayaev et al., 2007; Piron et al. 2016). The winter MLD and the associated θ, S and ρ properties were examined for the Labrador Sea and the SECF region by considering the profiles inside the cyan and pink boxes in Fig. 1, respectively. Those two boxes were defined to include all Argo profiles with MLD deeper than 700 m during 2016 – 2018 and the minimum of the monthly ADT for either the SECF region or the Labrador Sea. No deep MLD was recorded in the northernmost part of the Irminger Sea during this period. We computed the maximum MLD and the MLD third quartile (Q_3) from profiles with MLD greater than 700m in each of the two boxes separately. Q_3 is the MLD value that is exceeded by 25% of the profiles and is equivalent to the aggregate maximum depth of convection defined by Yashayaev and Loder (2016). The properties (ρ, θ and S) of the mixed layers were defined for each winter as the vertical mean from 200 m to the MLD of all profiles with MLD deeper than 700 m. For further use, we define the deep convection period as follows. For a given winter, the deep convection period begins the day when the first profile with a deep (>700m) mixed layer is detected and ends the day of the last detection of a deep mixed layer.

3.2. Time series of atmospheric forcing

The air-sea buoyancy flux (B_{surf}) was calculated as the sum of the contributions of Q and FWF (Gill, 1982; Billheimer & Talley, 2013). It reads:

166 $$B_{surf} = \frac{\alpha\, g}{\rho_0\, c_p}\, Q - \beta\, g\, SSS\, FWF \qquad \text{Eq. (1)}$$

167 Where α and β are the coefficients of thermal and saline expansions, respectively, estimated from

168 surface T and S. The gravitational acceleration g is equal to 9.8 m s^{-2}, the reference density of sea

169 water ρ_0 is equal to 1026 kg m^{-3} and heat capacity of sea water C_p is equal to 3990 J kg^{-1} °C^{-1}. SSS is

170 the sea surface salinity. Q and FWF are in W m^{-2} and m s^{-1}, respectively.

171 For easy comparison with previous results, which only considered the heat component of the

172 buoyancy air-sea flux (e.g. Yashayaev & Loder, 2017; Piron et al. 2017; Rhein et al., 2017), B$_{surf}$, in m^2

173 s^{-3}, was converted to W m^{-2} following Eq. (2) and noted B^{*}_{surf}

174 $$B^{*}_{surf} = \frac{\rho_0\, c_p}{g\, \alpha}\, B_{surf} \qquad \text{Eq. (2)}$$

175 The FWF was also converted to W m^{-2} using:

176 $$\text{FWF*} = \text{FWF}\ \beta\ SSS\ \frac{\rho_0\, c_p}{\alpha} \qquad \text{Eq. (3)}$$

177 We also computed the horizontal Ekman buoyancy flux (BF$_{ek}$), which can be decomposed into the

178 horizontal Ekman heat flux (HF$_{ek}$) and salt flux (SF$_{ek}$). Noting :

179 $$BF_{ek} = -g\, (U_e \partial_x SSD + V_e \partial_y SSD)\, \frac{c_p}{\alpha.g} \qquad \text{Eq. (4)}$$

180 $$HF_{ek} = -(U_e \partial_x SST + V_e \partial_y SST)\, \rho_0\, C_p \qquad \text{Eq. (5)}$$

181 $$SF_{ek} = -(U_e \partial_x SSS + V_e \partial_y SSS)\, \frac{\beta\ \rho_0\ C_p}{\alpha} \qquad \text{Eq. (6)}$$

182 BF$_{ek}$ = SF$_{ek}$ – HF$_{ek}$. U$_e$ and V$_e$ are the eastward and northward components of the Ekman horizontal

183 transport estimated from the wind stress meridional and zonal components. SSD, SST and SSS are ρ,

184 T and S at the surface of the ocean. BF$_{ek}$, HF$_{ek}$ and SF$_e$ are in J s^{-1} m^{-2}. Because ERA-Interim does not

185 supply SSD or SSS, they were estimated from EN4 as follows. The monthly T and S data at 5 m depth

186 from EN4 were interpolated on the same time and space grid as the air-sea fluxes from ERA-Interim

187 (12h and 0.75°, respectively). SSD was estimated from those interpolated EN4 data (SST and SSS).

188 Properties at 5 m depth were considered to be representative of the Ekman layer. Data at locations

189 where ocean bottom was shallower than 1000 m were excluded from the analysis to avoid regions

190 covered by sea-ice.

191 Following Piron et al. (2016), the time series of atmospheric forcing were estimated for the SECF

192 region and the Labrador Sea as follows. First, the gridded air-sea flux data and the horizontal Ekman

193 fluxes were averaged over the pink (SECF region) and cyan (Labrador Sea) boxes (Fig. 1). Second, we

194 estimated the accumulated fluxes from 1 September to 31 August the year after. Finally, we

195 computed the time series of the anomalies of the accumulated fluxes from 1 September to 31 August

196 with respect to the 1993 – 2016 mean.

197 Finally, in order to quantify the net intensity of the atmospheric forcing over the winter, we

198 computed estimates of B_{surf}* + BF_{ek} fluxes accumulated from 1 September to 31 March the year after.

199 Following Piron et al. (2017), the associated errors were calculated by a Monte Carlo simulation using

200 50 random perturbations of Q, FWF and B_{surf}. The error amounted to 0.05, 0.04 and 0.03 J m^{-2} for

201 B_{surf}*, Q and FWF*, respectively. The error of the horizontal Ekman buoyancy transport was also

202 estimated by a Monte Carlo simulation and amounted to 0.04 J m^{-2}.

203 3.3. Preconditioning of the water column

204 The preconditioning of the water column was evaluated as the buoyancy that has to be removed

205 $(B(zi))$ from the late summer density profile to homogenize it down to a depth zi. It reads:

206 $$B(zi) = \frac{g}{\rho_0} \, \sigma_0(zi)zi \, - \, \frac{g}{\rho_0} \int_{z_i}^{o} \sigma_0 \, (z)dz \qquad \text{Eq. (7)}$$

207 $\sigma_0(z)$ is the vertical profile of potential density anomaly estimated from the profiles of T and S

208 measured by Argo floats in September in the given region (pink or cyan box in Fig. 1).

209 Following Schmidt and Send (2007), we split B into a temperature (B_θ) and salinity (B_S) term:

210 $$B_\theta(zi) = -(\, g \, \alpha \, \theta(zi) \, zi \, - \, g \, \alpha \int_{zi}^{o} \theta(z) \, dz) \quad \text{Eq. (8)}$$

211 $$B_S(zi) = g \, \beta \, S(zi) \, zi \, - \, g \, \beta \int_{zi}^{o} S \, (z)dz \qquad \text{Eq. (9)}$$

212 In order to compare the preconditioning with the heat to be removed and/or air-sea heat fluxes, B,

213 B_θ and B_S are reported in J m^{-2}. B, B_θ and B_S were estimated for a given year from the mean of all

214 September profiles of B, B_θ and B_S. The associated errors were estimated as std(B)/√n, where n is

215 the number of profiles used to compute the September mean values.

216

217 4. RESULTS

218 4.1. Intensity of deep convection and properties of newly formed LSW

219   We examine the time-evolution of the winter mixed layer SECF since the exceptional convection

220   event of winter 2015 (W2015 hereinafter) (Table 1 and Figs. 1 - 3). In W2015, we recorded a

221   maximum MLD of 1,710 m south of Cape Farewell (Fig. 1a), in line with Piron et al. (2017). The

222   maximum MLD of 1,575 m observed for W2016 (Fig. 1b) is compatible with the MLD > 1,500 m

223   observed in a mooring array in the central Irminger Sea by de Jong et al. (2018). For W2015 and

224   W2016, Q3 was 1,205 m and 1,471 m, respectively (Table 1). In W2017, deep convection was

225   observed from three Argo profiles (Fig. 1c and Fig. 2a-c). The maximum MLD of 1,400 m was

226   observed on 16th March 2017 at 56.65°N – 42.30°W. In W2018, the maximum MLD of 1,300 m was

227   observed on 24 February at 58.12°N, 41.84°W (Fig. 1d, 2d-f). Float 5903102 measured MLD of 1,100

228   m South of Cape Farewell (Fig. 1d), but the estimated MLDs coincided with the deepest levels of

229   measurement of the float so that these estimates, possibly biased low (see Fig. 2d-f), were discarded

230   from our analysis. These results show that convection deeper than 1,300 m occurred during four

231   consecutive winters SECF.

232   Although the number of floats showing deep convection in W2017 and W2018 was small (3 and 2

233   floats), it represented a significant percentage of the floats operating in the SECF box at that time.

234   The percentage of floats showing deep convection in the SECF region was computed for the deep

235   convection periods defined from 15 January 2015 to 21 April 2015, 22 February 2016 to 21 March

236   2016, 16 March 2017 to 4 April 2017 and 24 February 2018 to 26 March 2018. The longest period of

237   deep convection occurred in W2015, the shortest in 2017. The percentage of floats showing deep

238   convection during the deep convection period are 73%, 50%, 33 % and 50%, for winters 2015, 2016,

239   2017 and 2018, respectively. The lowest % is found for W2017, but it is still substantial. It might

240   reflect that for this specific year floats showing deep MLD were found in the southwestern corner of

241   the SECF box only, suggesting that convection did not occur over the full box.

242   The properties (σ_0, S and θ) of the end of winter mixed layer were estimated for the four winters

243   (Table 1 and Fig. 3). We observed that, between W2015 and W2018, the water mass formed by deep

244   convection significantly densified and cooled by 0.019 kg m^{-3} and 0.215°C, respectively (see Table 1

245   and Fig. 3).

246   In the Labrador Sea, Q3 increased from 2015 to 2018 (see Table 1). Deep convection observed in the

247   Labrador Sea in W2018 was the most intense since the beginning of the Argo era (see Fig. 2c in

248   Yashayaev & Loder, 2016). From W2015 to W2018, newly formed LSW cooled, became saltier and

249   densified by 0.134°C, 0.013 and 0.023 kg m^{-3}, respectively (Table 1).

250   The water mass formed SECF is warmer and saltier than that formed in the Labrador Sea (Fig. 3). The

251   deep convection SECF is always shallower than in the Labrador Sea. This result is discussed later in

252   Sect. 5.

4.2. Analysis of the atmospheric forcing Southeast of Cape Farewell

254   The seasonal cycles of $B_{surf}*$ and Q are in phase and of the same order of magnitude, while FWF*,

255   which is positive and one order of magnitude lower than Q, does not present a seasonal cycle (Fig.

256   S3). The means (1993 – 2018) of the cumulative sums from 1 September to 31 March of Q, FWF* and

257    $B_{surf}*$ estimated over the SECF box (Fig. 1) are - 2.46 ± 0.43 x 10^9 J m^{-2}, 0.28 ± 0.10 x 10^9 J m^{-2} and -

258   2.22 ± 0.49 x 10^9 J m^{-2}, respectively. Despite $B_{surf}*$ is mainly explained by Q, the accumulated FWF*

259   amounts to ~10 % of the accumulated Q with opposite sign. The air-sea buoyancy flux is 10% lower

260   on average than the air-sea heat flux. Considering the Ekman transports, the 1993 – 2018 means of

261   the accumulated BF_{ek}, HF_{ek} and SF_{ek} from 1 September to 31 March amount to 0.37 ± 1.15 x 10^8 J m^{-2},

262   - 0.35 ± 1.36 x 10^8 J m^{-2}, and 0.02 ± 2.04 x 10^8 x 10^9 J m^{-2}, respectively. The horizontal Ekman heat

263   flux is negative, while the Ekman buoyancy flux is positive. This buoyancy gain indicates a

264   southeastward transport of surface freshwater caused by dominant winds from the southwest.

265   Noteworthy, BF_{ek} is one order of magnitude smaller than the $B_{surf}*$.

266   The total atmospheric forcing SECF was quantified as the sum of $B_{surf}*$ and BF_{ek}. The anomalies of

267   accumulated fluxes from 1 September to 31 August the year after, with respect to the mean 1993 –

268   2016, are displayed in Fig. 4 for the SECF box. The grey line in Fig. 4a is the total atmospheric forcing

269   anomaly ($B_{surf}*$ plus BF_{ek}). We identify years with very negative buoyancy loss in the SECF region, e.g.

270   1994, 1999, 2008, 2012 and 2015. The very negative anomalies of atmospheric forcing in 1999 and

271   2015 were caused by the very negative anomalies in both $B_{surf}*$ (Fig. 4a) and BF_{ek} (Fig.4d). This

272   correlation was not observed for all the years presenting a negative anomaly of atmospheric forcing.

273   Noteworthy, during W2016, W2017 and W2018, the anomaly of atmospheric forcing was close to

274   zero.

275   Contrary to the very negative anomaly in atmospheric fluxes over the SECF region observed for

276   W2015, the atmospheric fluxes were close to the mean during W2016, W2017 and W2018.

4.3. Analysis of the preconditioning of the water column Southeast of Cape Farewell

279   Our hypothesis is that the exceptional deep convection that happened in W2015 in the SECF region

280   favorably preconditioned the water column for deep convection the following winters. The time-

281   evolutions of θ, S, σ_1 and of $\Delta\sigma_1=0.01$ kg m^{-3} layer thicknesses (Fig. 5) show a marked change in the

282   hydrographic properties of the SECF region at the beginning of 2015 caused by the exceptional deep

283   convection that occurred during W2015 (see Piron et al., 2017). The intermediate waters (500 –

284   1,000 m) became colder than the years before and, despite a slight decrease in salinity, the cooling

285   caused the density to increase (Fig. 5c). Fig. 5d shows $\Delta\sigma_1=0.01$ kg m^{-3} layer thicknesses larger than

286   600 m appearing at the end of W2015 for the first time since 2002. In the density range 32.36 – 32.39

287   kg m^{-3}, these layers remained thicker than ~450 m during W2016 to W2018. This indicates low

288   stratification at intermediate depths and a favorable preconditioning of intermediate waters for deep

289   convection initiated by W2015 deep convection. The denser density of the core of the thick layers in

290   2017 -2018 compared with 2015 - 2016 agrees with the densification of the mixed layer SECF shown

291   in Table 1 and Fig. 3.

292   B(zi) is our estimate of the preconditioning of the water column before winter (see Method). Fig. 6a

293   shows that, deeper than 100 m, B for W2016, W2017 and W2018 was smaller than B for W2015 or B

294   for the mean W2008 – W2014. Furthermore, for W2016, W2017 and 2018, B remained nearly

295   constant with depth between 600 and 1,300 m, which means that once the water column has been

296   homogenized down to 600 m, little additional buoyancy loss results in the homogenization of the

297   water column down to 1,300 m. Both conditions (i) less buoyancy to be removed and (ii) absence of

298   gradient in the B profile down to 1,300 m indicate a more favorable preconditioning of the water

299   column for W2016, W2017 and W2018 than during W2008 – W2015.

300   To understand the relative contributions of θ and S to the preconditioning, we computed the thermal

301   (B_θ) and haline (B_S) components of B (B = B_θ + B_S). In general, B_θ (B_S) increases with depth when θ

302   decreases (S increases) with depth. On the contrary, a negative slope in a B_θ (B_S) profile corresponds

303   to θ increasing (S decreasing) with depth and is indicative of a destabilizing effect. The negative

304   slopes in B_θ and B_s profiles are not observed simultaneously because density profiles are stable.

305   We describe the relative contributions of B_θ and B_s to B by looking first at the mean 2008 – 2014

306   profiles (discontinuous blue lines in Fig. 6). B_θ accounts for most of the increase in B from the surface

307   to 800 m and below 1,400 m (see Fig. 6a and Fig. 6b). The negative slope in the B_s profile between

308   800 – 1,000 m (Fig. 6c) slightly reduces B (Fig. 6a) and is due to the decrease in S associated with the

309   core of LSW (see Fig. 3 in Piron et al. 2016). In the layer 1,000 – 1,400 m, the increase in B (Fig. 6a) is

310   mainly explained by the increase in B_s (Fig. 6c), which follows the increase in S in the transition from

311   LSW to Iceland Scotland Overflow Water (ISOW). This transition layer will be referred to hereinafter

312   as the deep halocline. The evaluation of the preconditioning of the water column was usually

313   analyzed in terms of heat (e.g., Piron et al. 2015; 2017). The decomposition of B in B_θ and B_s reveals

314   that θ governs B in the layer 0 – 800 m. S tends to reduce the stabilizing effect of θ in the layer 800 –

315   1,000 m, and reinforces it in the layer 1,000 – 1,400 m by adding up to 1×10^9 J m^2 to B.

316   In order to further understand why the SEFC region was favorably preconditioned during winters

317   2016 – 2018, we compare the B_θ and B_S of W2017, which was the most favorably preconditioned

318   winter, with the mean 2008 – 2014 (Fig. 7a). From the surface to 1,600 m, B_θ and B_S were smaller for

319   W2017 than for the mean 2008 – 2014. There are two additional remarkable features. First, in the

320   layer 500 – 1000 m, the large reduction of B_θ compared to the 2008 – 2014 mean, mostly explains

321   the decrease in B in this layer. Second, the more negative value of B_s in the layer 1,100 – 1,300 m,

322   compared to the 2008 – 2014 mean, eroded the B_θ slope, making the B profile more vertical for

323   W2017 than for the mean. The more negative contribution of B_s in the layer 1,100 – 1,300 m comes

324   from the fact that the deep halocline was deeper for W2017 (1,300 m, see orange dashed line in Fig.

325   7a) than for the mean 2008 – 2014 (1,000 m, see blue dashed line in Fig. 7a). Finally, we note that the

326   profiles of $B(z_i)$, $B_\theta(z_i)$ and $B_s(z_i)$ for W2016 and W2018 are more similar to the profiles of W2017 than

327   to those of W2015 or to the mean 2008 – 2014 (see Fig. 6), which indicates that the water column

328   was also favorably preconditioned for deep convection in W2016 and W2018 for the same reasons as

329   in W2017.

330   The origin of the changes in B is now discussed from the time evolutions of the monthly anomalies of

331   θ, S and σ_0 at 58°N – 40°W that is at the center of the SECF box (Fig. 8). The time evolutions there are

332   similar to those at any other location inside the SECF box. These anomalies were computed using

333   ISAS (Gaillard et al., 2016) and were referenced to the monthly mean of 2002 – 2016. A positive

334   anomaly of σ_0 appeared in 2014 between the surface and 600 m (Fig. 8a) and reached 1,200m in

335   2015 and beyond. This positive anomaly of σ_0 correlates with a negative anomaly of θ. The latter,

336   however, reached ~1,400 m depth in 2016 that is deeper than the positive anomaly of σ_0. The

337   negative anomaly of S between 1,000 - 1,500 m that appeared in 2015 and strongly reinforced in

338   2016 caused the negative anomaly in σ_0 between 1,200 – 1,500 m (the density anomaly caused by

339   the negative anomaly in θ between 1,200 – 1,400 m does not balance the density anomaly caused by

340   the negative anomaly of S).

341   The θ and S anomalies in the water column during 2016 – 2018 explain the anomalies of B, B_θ and B_s

342   and can be summarized as follows. On the one hand, the properties of the surface waters (down to

343   500 m) were colder than previous years and, despite they were also fresher, they were denser. The

344   density increase in the surface water reduced the density difference with the deeper-lying waters.

345   The intermediate layer (500 – 1000 m) was also favorably preconditioned due to the observed

346   cooling. Additionally, in the layer 1,100 – 1,300 m, the large negative anomaly of B_s with respect to its

347   mean is explained by the decrease in S in this layer, which caused a decrease in σ_0 and, consequently,

348   reduced the σ_0 difference with the shallower-lying water. The decrease in S also resulted in a

349   deepening of the deep halocline.

4.4. Atmospheric forcing versus preconditioning of the water column

351   We now use the estimates of the accumulated atmospheric forcing ($B_{surf}* + BF_{ek}$) from 1 September

352   to 31 March the year after (see Fig. S4) to predict the maximum convection depth for a given winter

353   based on September profiles of B. The predicted convection depth is determined as the depth at

354   which B(zi) (Fig. 6a) equals the accumulated atmospheric forcing. The associated error was estimated

355   by propagating the error in the atmospheric forcing (0.05×10^9 J m^{-2}). The accumulated atmospheric

356   forcing amounted to $-3.21 \times 10^9 \pm 0.05$ J m^{-2}, $-2.21 \pm 0.04 \times 10^9$ J m^{-2}, $-2.01 \pm 0.05 \times 10^9$ J m^{-2} and -2.47

357     $\pm 0.05 \times 10^9$ J m^{-2} for W2015, W2016, W2017 and W2018, respectively. We found predicted

358   convection depths of 1,085 ± 20 m, 1,285 ± 20 m, 1,415 ± 20 m and 1,345 ± 20 m for W2015, W2016,

359   W2017 and W2018, respectively. We consider Q3 as the observed estimate of the MLD (Table 1). The

360   predicted MLD agrees with the observed MLD within ± 200 m. The differences could be due to errors

361   in the atmospheric forcing (Josey et al., 2018), lateral advection and/or spatial variation in the

362   convection intensity within the box not captured by the Argo sampling.

363   The satisfactory predictability of the convection depth with our 1-D model indicates that deep

364   convection occurred locally. In spite the atmospheric forcing was close to mean (1993 – 2016)

365   conditions during W2016, W2017 and W2018, convection depths > 1300 m were reached in the SECF

366   region. This was only possible thanks to the favorable preconditioning.

367

5. DISCUSSION

369   Deep convection happens in the Irminger Sea and South of Cape Farewell during specific winters

370   characterized by a strong atmospheric forcing (high buoyancy loss), a favorable preconditioning (low

371   stratification) or both at the same time (Bacon et al., 2003; Pickart et al., 2003). In the Irminger Sea,

372   strong atmospheric forcing explained for instance the very deep convection (reaching depth greater

373   than 1,500 m) observed in the early 90s (Pickart, et al., 2003) and in W2015 (de Jong et al. 2016; Fröb

374   et al., 2016; Piron et al. 2017). It explained as well the return of deep convection in W2008 (Väge et

375   al., 2009) and in W2012 (Piron et al., 2016). The favorable preconditioning caused by the

376   densification of the mixed layer during W2008 favored a new deep convection event in W2009

377   despite neutral atmospheric forcing (de Jong et al. 2012). Similarly, the preconditioning observed

378   after W2015 in the SECF region favored deep convection in W2016 (this work). The favorable

379   preconditioning persisted three consecutive winters (2016 – 2018) in the SECF region, which allowed

380 deep convection although atmospheric forcing was close to the climatological values. Why did this
381 favorable preconditioning persist in time?

382 We previously showed that during 2016 − 2018 two hydrographic anomalies affected different
383 ranges of the water column in SECF box: a cooling intensified in the layer 200 − 800 m and a
384 freshening intensified in 1,000 − 1,500 m layer. Those resulted in a decrease in the vertical density
385 gradient between the intermediate and the deeper layers creating a favorable preconditioning of the
386 water column. Note that the cooling affected the layer from surface to 1,400 m and the freshening
387 affected the layer from near surface to 1,600 m, but the cooling and the freshening were intensified
388 at different depth ranges (Fig. 8).

389 We see in Fig. 5a a sudden decrease in θ in the intermediate layers in 2015 compared to the previous
390 years. It indicates that the decrease in θ of the intermediate layer likely originated locally during
391 W2015 when extraordinary deep convection happened. A slight freshening of the water column
392 (400- 1,500 m) appeared in 2015, likely caused by the W2015 convection event, then it decreased
393 before a second S anomaly intensified in 2016 between 1,100 and 1,400 m (Fig. 8c). It is unlikely that
394 this second anomaly was exclusively locally formed by deep convection because it intensified during
395 summer 2016. Our hypothesis is that this second S anomaly originated in the Labrador Sea and was
396 further transferred to the SECF region by the cyclonic circulation encompassing the Labrador Sea and
397 Irminger Sea at these depths (Daniault et al., 2016; Ollitrault & Colin de Verdière, 2014; Lavander et
398 al., 2000 ; Straneo et al., 2003). It is corroborated by the 2D evolution of the anomalies in S in the
399 layer 1,200 − 1,400 m (Fig. 9): a negative anomaly in S appeared in the Labrador Sea in February
400 2015, which was transferred southward and northeastward in February 2016 and intensified over the
401 whole SPNA in February 2017. By this mechanism, the advection from the Labrador Sea contributed
402 to create property anomalies in the water column. However, the buoyancy budget showed that this
403 was a minor contribution compared to the buoyancy loss due to the local air-sea flux, even if it was
404 essential to preconditioning the water column for deep convection.

405 We now compare the atmospheric forcing and the preconditioning of the water column in the SECF
406 region with those of the nearby Labrador Sea where deep convection happens almost every year.
407 The atmospheric forcing over the Labrador Sea is ~15 % larger than that over the SECF region: the
408 means (1993 - 2018) of the atmospheric forcing, defined as the time accumulated $B_{surf}* + BF_{ek}$ from 1
409 September to 31 March the year after, are -2.61 ± 0.55 x 10^9 J m^{-2} in the Labrador Sea and -2.18 ±
410 0.54 x 10^9 J m^{-2} in the SECF region. The difference was larger during the period 2016 − 2018 when the
411 atmospheric forcing equaled -3.10 ± 0.19 x 10^9 J m^{-2} in the Labrador Sea and -2.23 ± 0.23 x 10^9 J m^{-2} in
412 the SECF region. In terms of preconditioning, the 2008 − 2014 mean B profile (blue continuous lines

413   in Fig. 7) was lower by ~0.5 x 10^9 J m^{-2} in the Labrador Sea than SECF for the surface to 1,000 m layer

414   and by more than 1 x 10^9 J m^{-2} below 1,200 m. It indicates that the water column was more favorably

415   preconditioned in the Labrador Sea than in the SECF region during 2008 – 2014. Differently, B for

416   W2017 shows slightly lower values from the surface to 1,300 m in the SECF region than in the

417   Labrador Sea (see orange lines in Fig. 7). However, B in the Labrador Sea remains constant down to

418   the depth of the deep halocline between LSW and North Atlantic Deep Water (NADW) at 1,700 m. In

419   the SECF region, the deep halocline remained at ~1,300 m between 2016 and 2018 (see B_s lines in

420   Fig. 7a). Differently, in the Labrador Sea, the deep halocline deepened from 1,200 m for the mean to

421   1,735 m, 1,775 m and 1905 m in W2016, W2017 and W2018, respectively (see dashed lines in Fig.

422   7b). The deep halocline acts as a physical barrier for deep convection in both the SECF region and the

423   Labrador Sea, but because the deep halocline is deeper in the Labrador Sea than in SECF region, the

424   preconditioning is more favorable to a deeper convection in the Labrador Sea than in the SECF

425   region. Summarizing, in winters 2016 - 2018 in the Labrador Sea, both atmospheric forcing and

426   preconditioning of the water column granted the deepest convection depth in the Labrador Sea since

427   the beginning of the Argo period (comparison of our results with those of Yashayaev and Loader,

428   2017). Contrasting, in SECF region, during the same period, the atmospheric forcing was close to

429   climatological values, and the favorable preconditioning of the water column allowed 1,300 m depth

430   convection, what was exceptional for the SECF region.

431   The Labrador Sea, SECF region and Irminger Sea are three distinct deep convection sites (e.g.

432   Yashayaev et al., 2007; Bacon et al., 2003; Pickart et al., 2003; Piron et al., 2017). In this work, we

433   give new insights on the connections between the different sites, showing how lateral advection of

434   fresh LSW formed in the Labrador Sea favored the preconditioning in the SECF region fostering

435   deeper convection.

436   Climate models forecast increasing input of freshwater in the North Atlantic due to ice-melting under

437   present climate change (Bamber et al., 2018), which could reduce, or even shut-down, the deep

438   convection in the North Atlantic (Yang et al., 2016; Brodeau & Koenigk, 2016). We observed a fresh

439   anomaly in the surface waters in regions close to the eastern coast of Greenland in 2016 that

440   extended to the whole Irminger Sea in 2017 (Fig. S6). However, this surface freshening did not

441   hamper the deep convection in the SECF region possibly because the surface water also cooled.

442   Swingedouw et al., 2013 indicated that the freshwater signal due to Greenland ice sheet melting is

443   mainly accumulating in the Labrador Sea. However, no negative anomaly of S was detected in the

444   surface waters of the Labrador Sea (Fig. S6). It might be explained by the intense deep convection

445   affecting the Labrador Sea since 2014 that could have transferred the surface freshwater anomaly to

446   the ocean interior. This suggests that, in the last years, the interactions between expected climate

447 change anomalies and the natural dynamics of the system combined to favor very deep convection.

448 This however does not foretell the long term response to climate change.

449

6. CONCLUSIONS

451 During 2015 – 2018 winter deep convection happened in the SECF region reaching deeper than 1,300

452 m. It is the first time deep convection was observed in this region during four consecutive winters.

453 The atmospheric forcing and preconditioning of the water column was evaluated in terms of

454 buoyancy. We showed that the atmospheric forcing is 10% weaker when evaluated in terms of

455 buoyancy than in terms of heat because of the non-negligible effect of the freshwater flux. The

456 analysis of the preconditioning of the water column in terms of buoyancy to be removed (B) and its

457 thermal and salinity terms (B_θ and B_s) revealed that B_θ dominated the B profile from the surface to

458 800 m and B_s reduced the B in the 800 – 1000 m layer because of low salinity of LSW. Deeper, B_s

459 increased B due to the deep halocline (LSW-ISOW) that acted as a physical barrier limiting the depth

460 of the convection.

461 During 2016 – 2018, the air-sea buoyancy losses were close to the climatological values and the very

462 deep convection was possible thanks to the favorable preconditioning of the water column. It was

463 surprising that these events reached convection depths similar to those observed in W2012 and

464 W2015, when the latter were provoked by high air-sea buoyancy loss intensified by the effect of

465 strong wind stress. It was also surprising that the water column remained favorably preconditioned

466 during three consecutive winters without strong atmospheric forcing. In this paper, we studied the

467 reasons why this happened.

468 The preconditioning for deep convection during 2016 – 2018 was particularly favorable due to the

469 combination of two types of hydrographic anomalies affecting different depth ranges. First, the

470 surface and intermediate waters (down to 800 m) were favorably preconditioned because buoyancy

471 (density) decreased (increased) due to the cooling caused by the atmospheric forcing. Second,

472 buoyancy (density) increased (decreased) in the layer 1,200 – 1,400 m due to the decrease in S

473 caused by the lateral advection of fresher LSW formed in the Labrador Sea. The S anomaly of this

474 layer resulted in a deeper deep halocline. Hence, the cooling of the intermediate water was essential

475 to reach convection depth of 800 – 1,000 m, and the freshening in the layer 1,200 – 1,400 m and the

476 associated deepening of the deep halocline, allowed the very deep convection (> 1,300 m) in W2016

477 – W2018.

478 **Author contribution**: PZ treated and analyzed the data. PZ and HM interpreted the results. PZ, HM

479 and VT discussed the results and wrote the paper.

480 **ACKNOWLEDGEMENT**

481 The Argo data were collected and made freely available by the International Argo Program and the

482 national programs that contribute to

483 it. (http://www.argo.ucsd.edu, http://argo.jcommops.org). The Argo Program is part of the Global

484 Ocean Observing System. The NAO data were downloaded from the UCAR Climate Data Guide

485 website (Schneider et al., 2013): https://climatedataguide.ucar.edu/climate-data/hurrell-north-

486 atlantic-oscillation-nao-index-pc-based. The Ssalto/Duacs altimeter products were produced and

487 distributed by the Copernicus Marine and Environment Monitoring Service (CMEMS)

488 (http://www.marine.copernicus.eu).

489

490 **REFERENCES**

491 Argo Data Management Team: Argo user's manual V3.2. https://doi.org/10.13155/29825, 2017

492 Argo group: Argo float data and metadata from Global Data Assembly Centre (Argo GDAC),

493 SEANOE, https://doi.org/10.17882/42182 ,2019

494 Bacon, S.: Circulation and Fluxes in the North Atlantic between Greenland and Ireland. *Journal of*

495 *Physical Oceanography*, *27*(7), 1420–1435. *https://doi.org/10.1175/1520-*

496 *0485(1997)027<1420:CAFITN>2.0.CO;2*, 1997.

497 Bacon, S., Gould, W. J. and Jia, Y.: Open-ocean convection in the Irminger Sea, Geophys. Res. Lett.,

498 30(5), 1246, doi:10.1029/2002GL016271, 2003.

499 Bamber, J. L., Tedstone, A. J., King, M. D., Howat, I. M., Enderlin, E. M., van den Broeke, M. R., & Noel,

500 B.: Land Ice Freshwater Budget of the Arctic and North Atlantic Oceans: 1. Data, Methods, and

501 Results, *Journal of Geophysical Research: Oceans*, 1–11,

502 https://doi.org/10.1002/2017JC013605, 2018.

503 Billheimer, S., & Talley, L. D.: Near cessation of Eighteen Degree Water renewal in the western North

504 Atlantic in the warm winter of 2011 – 2012, *118*(November), 6838–6853,

505 https://doi.org/10.1002/2013JC009024, 2013.

506 Brodeau, L., & Koenigk, T.: Extinction of the northern oceanic deep convection in an ensemble of

507   climate model simulations of the 20th and 21st centuries, *Climate Dynamics*, *46*(9–10), 2863–

508   2882. https://doi.org/10.1007/s00382-015-2736-5, 2016.

509 Centurioni and Gould, W. J.: Winter conditions in the Irminger Sea observed with profiling floats,

510   *Journal of Marine Research*, 62, 313–336, 2004.

511 Daniault, N., Mercier, H., Lherminier, P., Sarafanov, A., Falina, A., Zunino, P., Gladyshev, S. : The

512   northern North Atlantic Ocean mean circulation in the early 21st century, *Progress in*

513   *Oceanography*, *146*(June), 142–158, https://doi.org/10.1016/j.pocean.2016.06.007, 2016.

514 de Boyer Montégut, C., Madec, G., Fischer, A. S., Lazar, A., & Iudicone, D.: Mixed layer depth over the

515   global ocean: An examination of profile data and a profile-based climatology, *Journal of*

516   *Geophysical Research C: Oceans*, *109*(12), 1–20, https://doi.org/10.1029/2004JC002378, 2004.

517 de Jong, M.F., Oltmanns, M., Karstensen, J., and de Steur, L.: Deep Convection in the Irminger Sea

518   Observed with a Dense Mooring Array, *31*(February), 50–59,

519   https://doi.org/10.5670/oceanog.2018.109, 2018.

520 de Jong, M. F., & de Steur, L.: Strong winter cooling over the Irminger Sea in winter 2014–2015,

521   exceptional deep convection, and the emergence of anomalously low SST, *Geophysical*

522   *Research Letters*, *43*(13), 7106–7113. https://doi.org/10.1002/2016GL069596, 2016.

523 de Jong, M. F., Van Aken, H. M., Våge, K., & Pickart, R. S.: Convective mixing in the central Irminger

524   Sea: 2002-2010, *Deep-Sea Research Part I: Oceanographic Research Papers*, *63*, 36–51.

525   https://doi.org/10.1016/j.dsr.2012.01.003, 2012.

526 Dee, D. P., Uppala, S. M., Simmons, A. J., Berrisford, P., Poli, P., Kobayashi, S., Vitart, F.: The ERA-

527   Interim reanalysis: Configuration and performance of the data assimilation system, *Quarterly*

528   *Journal of the Royal Meteorological Society*, *137*(656), 553–597. https://doi.org/10.1002/qj.828,

529   2011.

530 Fröb, F., Olsen, A., Våge, K., Moore, G.W.K., Yashayaev, I., Jeansson, E. & Rajasakaren B.: Irminger Sea

531   deep convection injects oxygen and anthropogenic carbon to the ocean interior. NATURE

532   COMMUNICATIONS | 7:13244 |

533   DOI:10.1038/ncomms13244|www.nature.com/naturecommunications, 2016.

534 Gaillard, F., Reynaud, T., Thierry, V., Kolodziejczyk, N., & Von Schuckmann, K.: In situ-based reanalysis

535   of the global ocean temperature and salinity with ISAS: Variability of the heat content and steric

536   height. *Journal of Climate*, *29*(4), 1305–1323. https://doi.org/10.1175/JCLI-D-15-0028.1, 2016.

537   Gill, A. E. (1982), Atmosphere-Ocean Dynamics, vol. 30, Academic, San Diego, CA.

538

539   Good, S. A., Martin, M. J., & Rayner, N. A.: EN4: Quality controlled ocean temperature and salinity

540   profiles and monthly objective analyses with uncertainty estimates. *Journal of Geophysical*

541   *Research: Oceans*, *118*(12), 6704–6716. https://doi.org/10.1002/2013JC009067, 2013.

542   Josey, S. A., Hirschi, J. J.-M., Sinha, B., Duchez, A., Grist, J. P., Marsh, R.: The Recent Atlantic Cold

543   Anomaly: Causes, Consequences, and Related Phenomena. Annual Review of Marine Science,

544   10 (1). 475-501.https://doi.org/10.1146/annurev-marine-121916-063102, 2018

545   Kieke, D., & Yashayaev, I.: Studies of Labrador Sea Water formation and variability in the subpolar

546   North Atlantic in the light of international partnership and collaboration. *Progress in*

547   *Oceanography*, *132*, 220–232. https://doi.org/10.1016/j.pocean.2014.12.010, 2015a.

548   Kieke, D., & Yashayaev, I.: Studies of Labrador Sea Water formation and variability in the subpolar

549   North Atlantic in the light of international partnership and collaboration, *Progress in*

550   *Oceanography*, *132*, 220–232, https://doi.org/10.1016/j.pocean.2014.12.010, 2015b.

551   Kolodziejczyk, N., Prigent-Mazella A., and Gaillard F. (2017). ISAS-15 temperature and salinity gridded
552   fields**. SEANOE**. http://doi.org/10.17882/52367

553   Lavender, K. L.,Davis, R. E., & Owens, W. B.: Mid-depth recirculation observed in the interior

554   Labrador and Irminger seas by direct velocity measurements. NATURE |VOL 407 | 7

555   SEPTEMBER 2000 |www.nature.com, 2000.

556   Marshall, J., & Schott, F.: Open-Ocean Convection ' Theory , and Models Observations ,. *Reviews of*

557   *Geophysics*, *37*(98), 1–64. https://doi.org/10.1029/98RG02739, 1999.

558   Ollitrault, M., & Colin de Verdière, A.: The Ocean General Circulation near 1000-m Depth, *Journal of*

559   *Physical Oceanography*, *44*(1), 384–409. https://doi.org/10.1175/JPO-D-13-030.1, 2014.

560   Pickart, R. S., orres, D. J. T and Clarke, R. A.: Hydrography of the Labrador Sea during active

561   convection, J. Phys. Oceanogr., 32, 428–457, 2002.

562   Pickart, R. S., Straneo, F., & Moore, G. W. K.: Is Labrador Sea Water formed in the Irminger basin?

563   *Deep-Sea Research Part I: Oceanographic Research Papers*, *50*(1), 23–52,

564   https://doi.org/10.1016/S0967-0637(02)00134-6, 2003.

565   Piron, A., Thierry, V., Mercier, H., & Caniaux, G.: Argo float observations of basin-scale deep

566   convection in the Irminger sea during winter 2011–2012. *Deep-Sea Research Part I:*

567   *Oceanographic Research Papers*, *109*, 76–90. https://doi.org/10.1016/j.dsr.2015.12.012, 2016.

568 Piron, A., Thierry, V., Mercier, H., & Caniaux, G.: Gyre-scale deep convection in the subpolar North
569   Atlantic Ocean during winter 2014–2015. *Geophysical Research Letters*, *44*(3), 1439–1447.
570   https://doi.org/10.1002/2016GL071895, 2017.

571 Rhein, M, Steinfeldt, R, Kieke, D, Stendardo, I and Yashayaev, I.: Ventilation variability of Labrador
572   Sea Water and its impact on oxygen and anthropogenic carbon: a review, *Philosophical
573   Transactions of the Royal Society A: Mathematical, Physical and Engineering Sciences*,
574   375(2102). 20160321. doi:10.1098/rsta.2016.0321, 2017.

575 Schmidt, S., & Send, U.: Origin and Composition of Seasonal Labrador Sea Freshwater, *Journal of
576   Physical Oceanography*, *37*(6), 1445–1454. https://doi.org/10.1175/JPO3065.1, 2007.

577 Straneo, F, Pickart, R.S., Lavender, K.: Spreading of Labrador sea water: an advective-diffusive study
578   based on Lagrangian data. Deep-Sea Research Part I-Oceanographic Research Papers. 50:701-
579   719, 2003.

580 Swingedouw, D., Rodehacke, C. B., Behrens, E., Menary, M., Olsen, S. M., & Gao, Y.: Decadal
581   fingerprints of freshwater discharge around Greenland in a multi-model ensemble, 695–720.
582   https://doi.org/10.1007/s00382-012-1479-9, 2013.

583 Yang, Q., Dixon, T. H., Myers, P. G., Bonin, J., Chambers, D., & Van Den Broeke, M. R.: Recent
584   increases in Arctic freshwater flux affects Labrador Sea convection and Atlantic overturning
585   circulation, *Nature Communications*, *7*, 1–7. https://doi.org/10.1038/ncomms10525, 2016.

586 Yashayaev, I., Bersch, M., & van Aken, H. M.: Spreading of the Labrador Sea Water to the Irminger
587   and Iceland basins, *Geophysical Research Letters*, *34*(10), 1–8.
588   https://doi.org/10.1029/2006GL028999, 2007.

589 Yashayaev, I., & Clarke, A.: Evolution of North Atlantic Water Masses Inferred From Labrador Sea
590   Salinity Series, *Oceanography*, *21*(1), 30–45. https://doi.org/10.5670/oceanog.2008.65, 2008.

591 Yashayaev, I., & Loder, J. W.: Recurrent replenishment of Labrador Sea Water and associtated
592   decadal-scale variability, *Journal Geophysical Research: Oceans*, *121*, 8095–8114,
593   https://doi.org/10.1002/2016JC012046, 2016.

594 Yashayaev, I., & Loder, J. W.: Further intensification of deep convection in the Labrador Sea in 2016.
595   *Geophysical Research Letters*, *44*(3), 1429–1438. https://doi.org/10.1002/2016GL071668, 2017.

596

Table 1. Properties of the deep convection SECF and in the Labrador Sea in winters 2015 – 2018. We
show: the maximal MLD observed, the aggregate maximum depth of convection Q3, the σ_0, S and θ
of the winter mixed layer formed during the convection event and n, which is the number of Argo
profiles indicating deep convection. The uncertainties given with σ_0, S and θ are the standard
deviation of the n values considered to estimate the mean values.

SECF	Maximal MLD (m)	Q3 MLD (m)	σ_0	Salinity	θ	n
W2015	1710	1205	27.733 ± 0.007	34.866± 0.013	3.478 ± 0.130	29
W2016	1575	1471	27.746± 0.002	34.871± 0.003	3.388 ± 0.032	3
W2017	1400	1251	27.745± 0.007	34.868± 0.007	3.364± 0.109	3
W2018	1300	1300	27.748± 0.001	34.859± 0.003	3.263± 0.031	2
LABRADOR SEA	Maximal MLD	Q3 MLD	σ_0	Salinity	θ	n
W2015	1675	1504	27.733 ± 0.009	34.842 ± 0.010	3.279 ± 0.036	41
W2016	1801	1620	27.743 ± 0.006	34.836 ± 0.010	3.124 ± 0.047	18
W2017	1780	1674	27.752 ± 0.008	34.853 ± 0.009	3.172 ± 0.029	26
W2018	2020	1866	27.756 ± 0.006	34.855 ± 0.010	3.145 ± 0.083	13

602

603

604

605

606

608
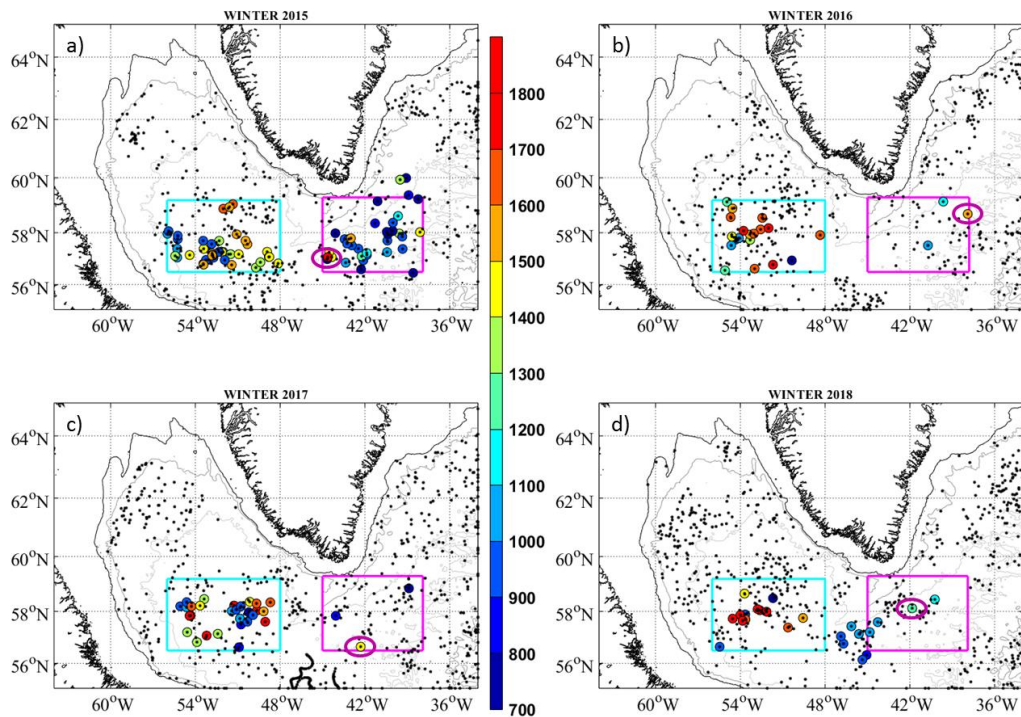
609 **Figure 1.** Positions of all Argo float north of 55°N in the Atlantic between 1 January and 30 April a)
610 2015, b) 2016, c) 2017 and d) 2018 (black and colored points). The colored points and color bar
611 indicate the mixed layer depth (MLD) when MLD was deeper than 700 m. The pink circles indicate
612 the position of the maximal MLD observed SECF each winter. The pink and cyan boxes delimit the
613 regions used for estimating the time series of atmospheric forcing and the vertical profiles of
614 buoyancy to be removed in the SECF region and the Labrador Sea, respectively (SECF: 56.5°N –
615 59.3°N and 45.0°W – 38.0°W, Labrador Sea: 56.5°N – 59.2°N and 56°W – 48°W).

616
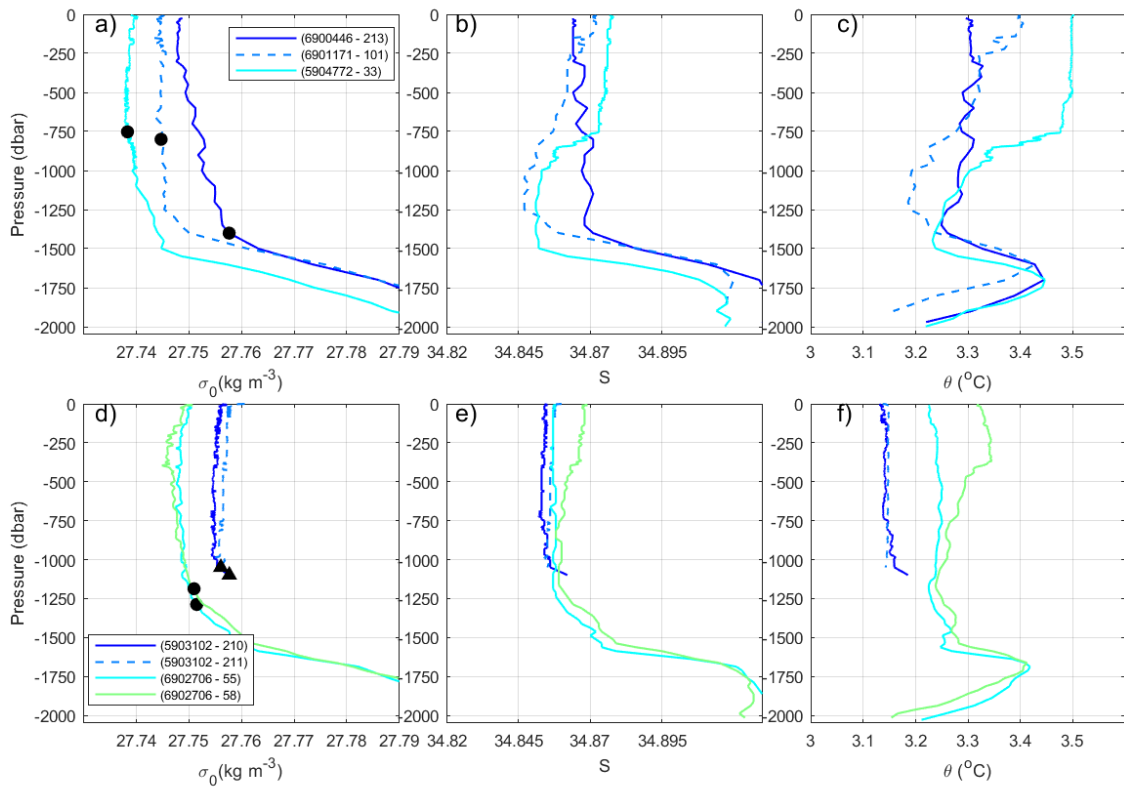
Figure 2. Vertical distribution of σ_0, S and θ of Argo profiles showing MLD deeper than 700 m SECF in Winter 2017 (a, b and c) and in Winter 2018 (d, e, f). The black points indicate the MLD. The triangles in d) are the MLD which coincided with the maximal profiling pressure reached by the float. In the legend, the float and cycle of each profile are indicated.

621
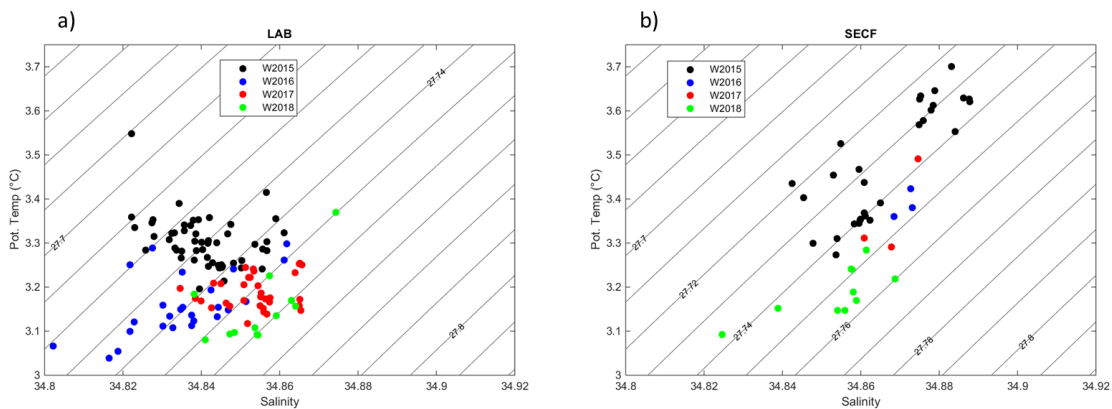
Figure 3. TS diagrams in the mixed layer for profiles with MLD deeper than 700 m during winters 2015, 2016, 2017 and 2018 for a) the Labrador Sea and b) SECF. The properties of the mixed layers were estimated as the vertical means between 200 m and the MLD.
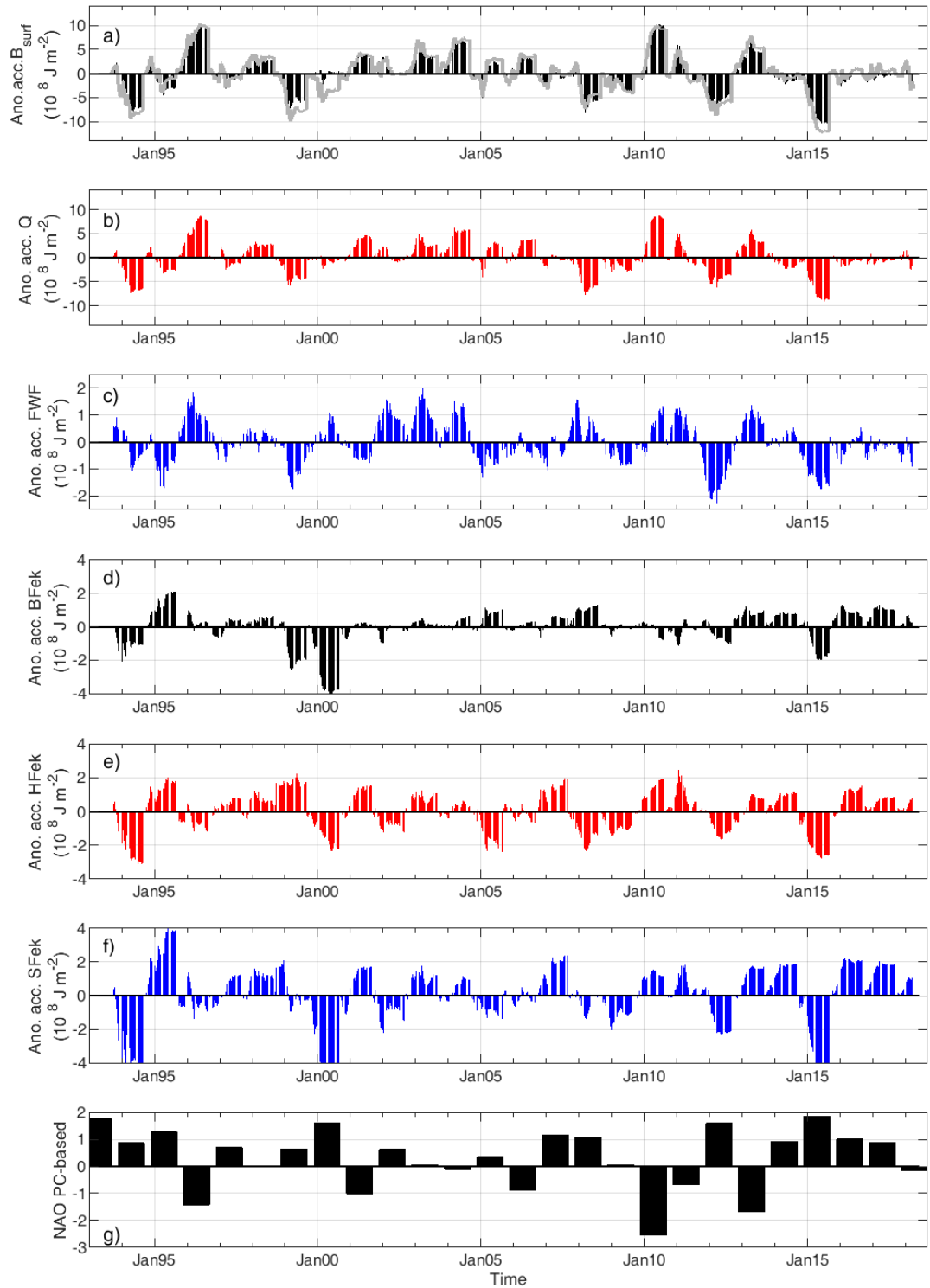
625
626 **Figure 4.** Time series of anomalies of accumulated a) Bsurf*, b) Q, c) FWF* d) BF$_{ek}$,e) HF$_{ek}$ and f) SF$_{ek}$,

averaged in the SECF region. They are anomalies with respect to 1993 – 2016. The accumulation was from 1 September to 31 August the following year. The winter NAO index (Hurrel et al., 2018) is also represented in g). Gray line in a) is the sum of the anomalies of accumulated $B_{surf}*$ and BF_{ek}. Note that the range of values in the y-axis is not the same in all the plots.
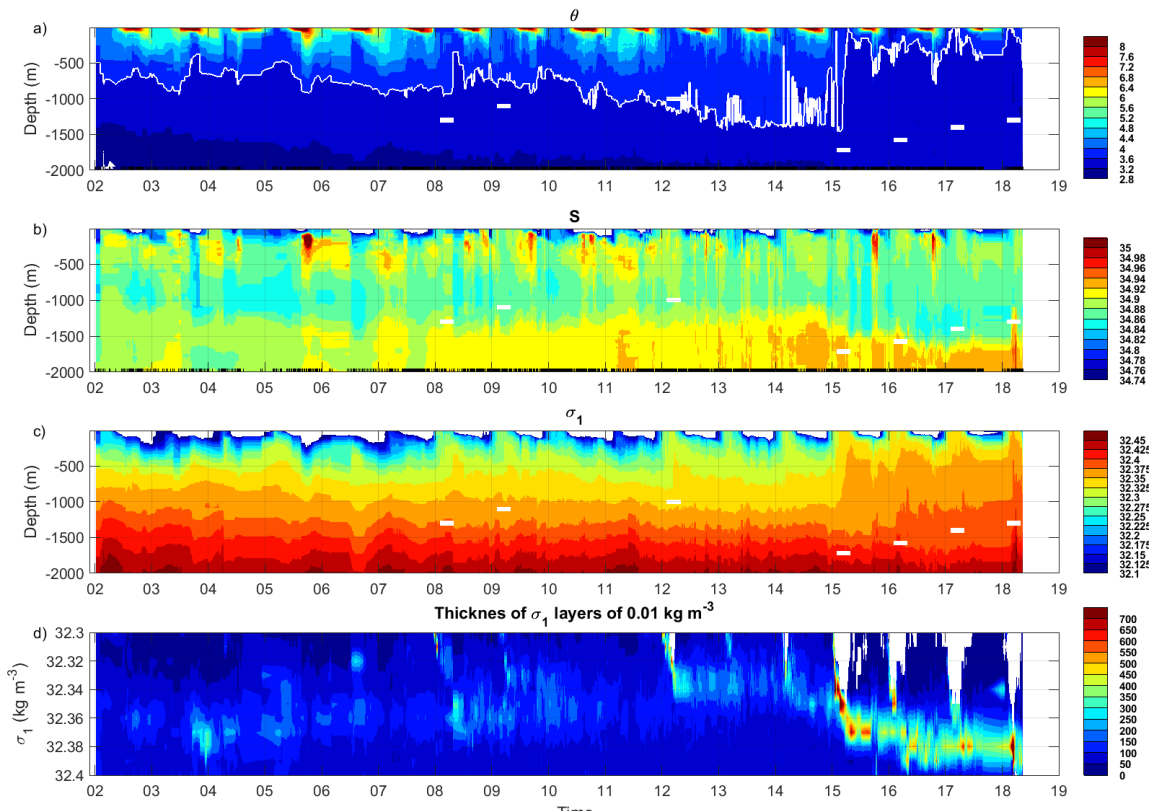
Figure 5. Time-evolutions of vertical profiles measured from Argo floats in the SECF region: a) θ ; b) S; c) σ_1 and d) thickness of 0.01 kg m^{-3} thick σ_1 layers. The white horizontal bars in plots a), b) and c) indicate the maximal convection depth observed in Irminger Sea or SECF when deep convection occurred. The white line in plot a) indicates the depth of the isotherm 3.6 °C. The black vertical ticks on the x-axes of plot b) indicate times of Argo measurements. These figures were created from all Argo profiles reaching deeper than 1000 m in the SECF region (56.5° – 59.3°N, 45°– 38°W, pink box in Fig. 1). The yearly numbers of Argo profiles used in this figure are shown in Fig. S5.

641
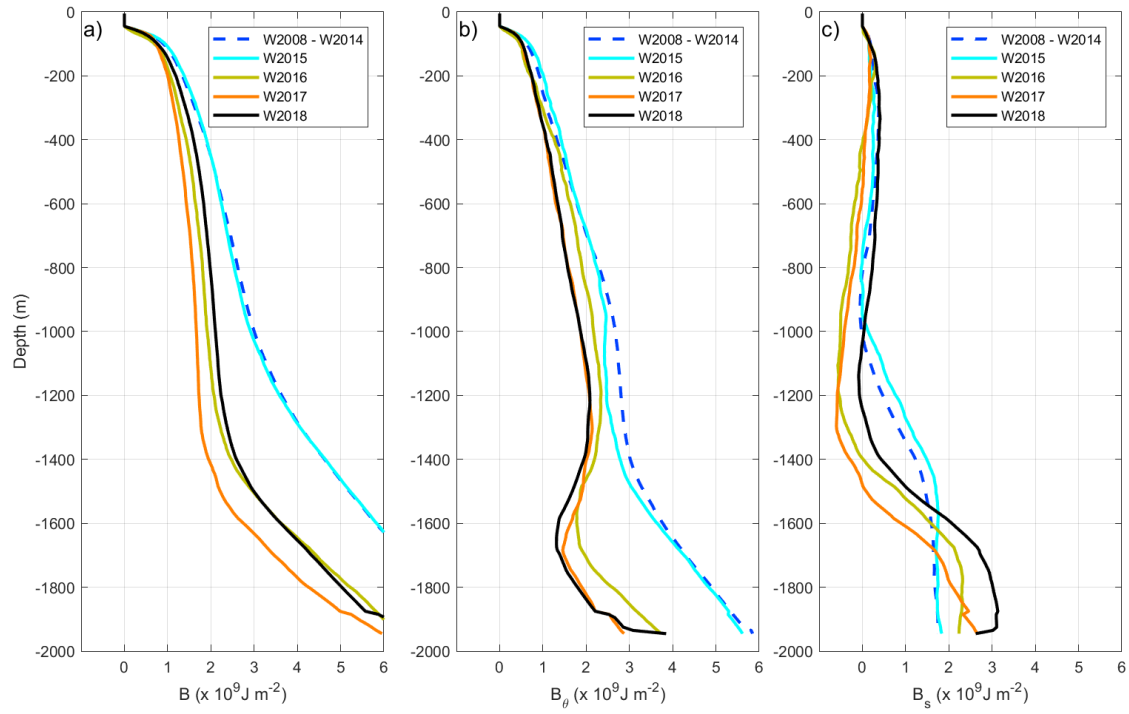
Figure 6. Vertical profile of a) the buoyancy to be removed (B), b) the thermal component (B_θ) and c) the salinity component (B_s). They were calculated from all Argo data measured in the SECF box (see Fig. 1) in September before the winter indicated in the legend. For W2015 and W2018, we considered data from 15/08/2017 to 30/09/2017 because not enough data were available in September. The number of Argo profiles taken into account to estimate the B profiles was more than ten for all the winters.

648
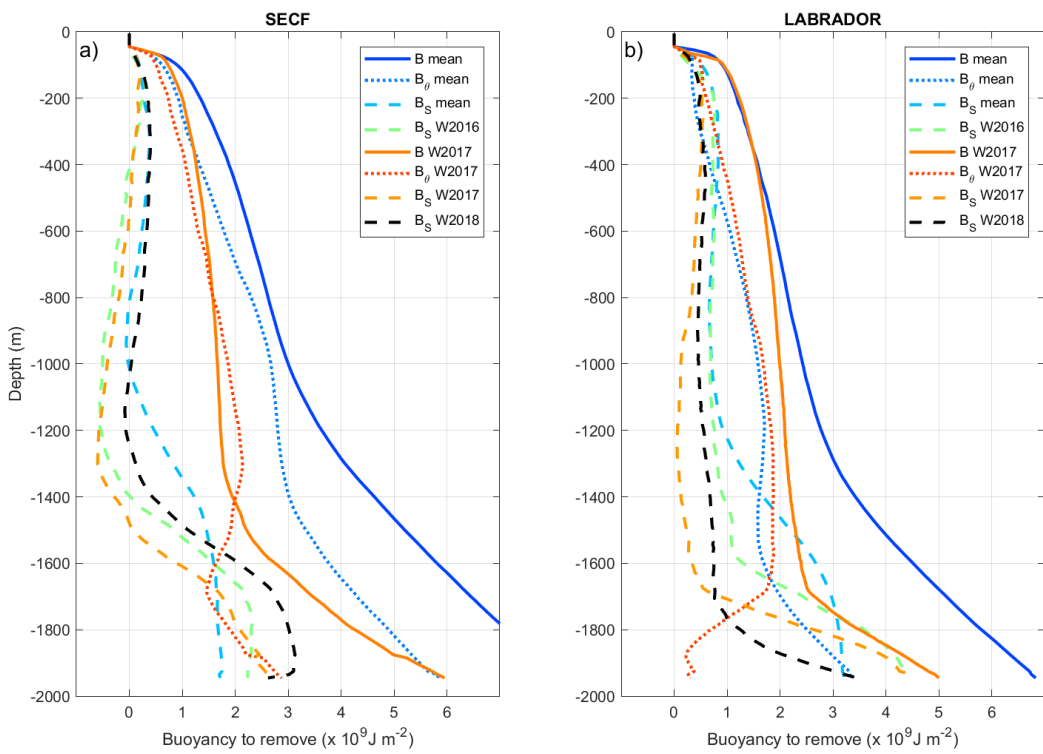
Figure 7. Decomposition of profiles of buoyancy to be removed (B, continuous lines) in its thermal

(B_θ, dotted lines) and salinity (B_s, dashed lines) components in a) the SECF region; b) the Labrador

Sea. The B_s components for W2016 and W2018 were added to show the evolution of the depth of

the deep halocline.

653

654

655

656
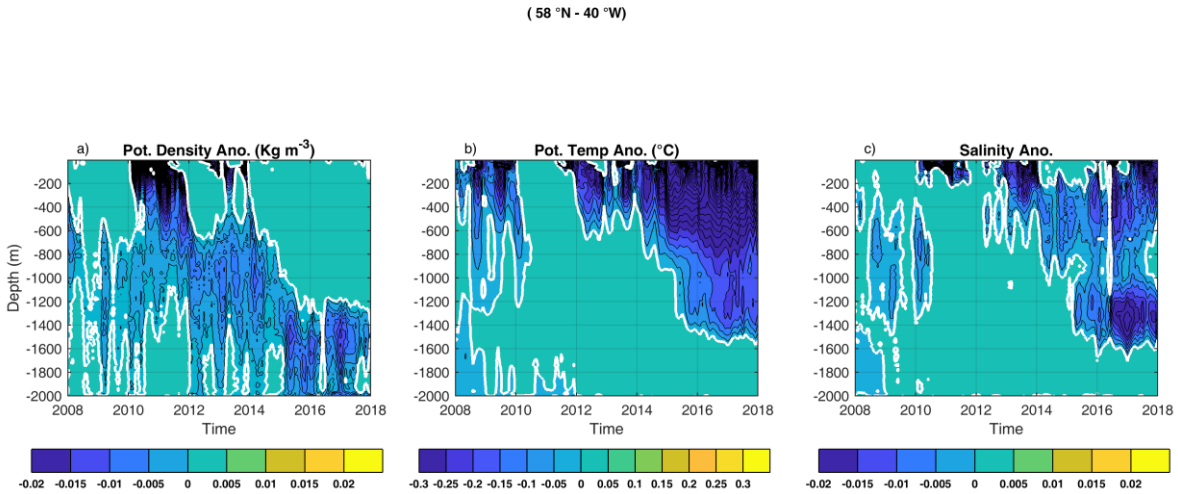
Figure 8. Evolution of vertical profiles of monthly anomalies of a) σ_0, b) θ and c) S, at 58°N, 40°W. The anomalies were estimated from the ISAS database (Gaillard et al., 2016), and were referenced to the monthly mean estimated for 2002 – 2016.
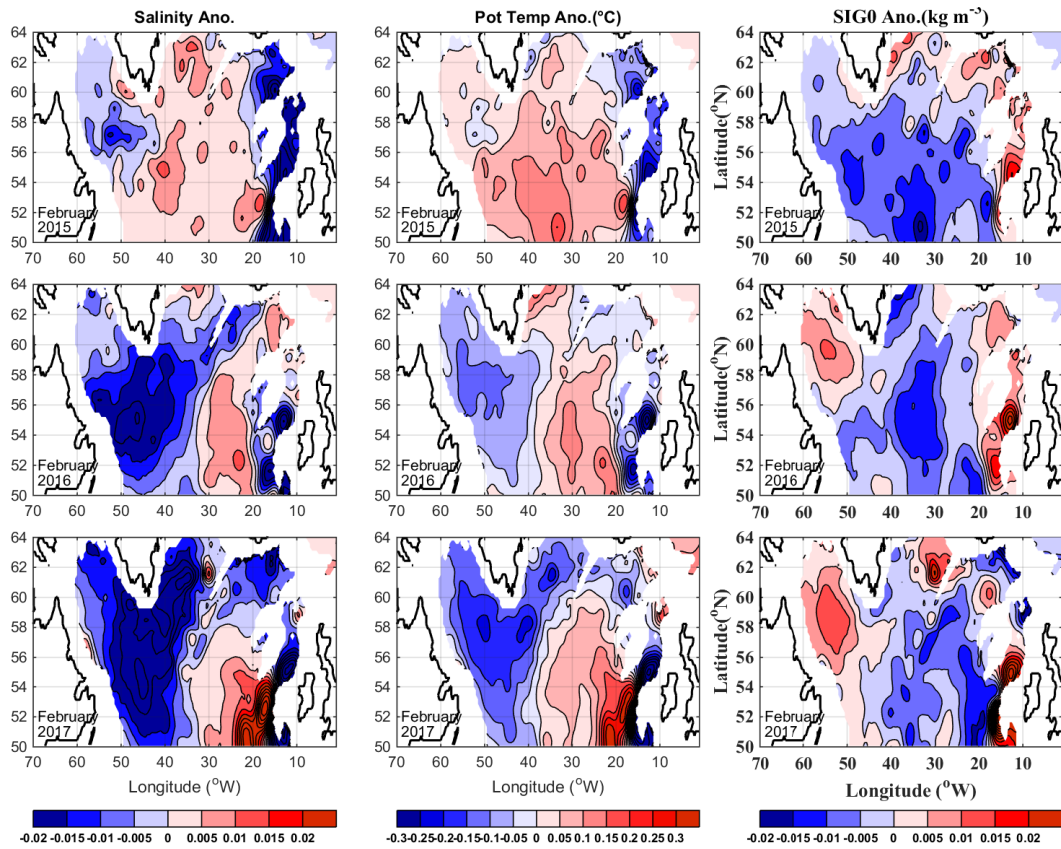
660
661 **Figure 9.** Horizontal distribution of the anomalies of S (left panels), θ (central panels) and σ_0 (right panels) in the layer 1200 – 1400 m in February 2015 (upper panels), February 2016 (central panels) and February 2017 (lower panels). The monthly anomalies were estimated from ISAS database and are referenced to the period 2002 – 2016.